Acoustic waves scattered by elastic waveguides using a spectral approach with a 2.5D coupled boundary-finite element method

F.J. Cruz-Muñoz[a], A. Romero[a,*], P. Galvín[a], A. Tadeu[b,c]

[a]*Escuela Técnica Superior de Ingeniería, Universidad de Sevilla, Camino de los Descubrimientos, 41092 Sevilla, Spain*
[b]*ITeCons - Institute for Research and Technological Development in Construction, Energy, Environment and Sustainability, Rua Pedro Hispano s/ n., 3030-289 Coimbra, Portugal*
[c]*ADAI - LAETA, Department of Civil Engineering, University of Coimbra, Pólo II, Rua Luís Reis Santos, 3030-788 Coimbra, Portugal*

Abstract

This work presents a two-and-a-half dimensional (2.5D) spectral formulation based on the finite element method (FEM) and the boundary element method (BEM) to study wave propagation in acoustic and elastic waveguides. The analysis involved superposing two dimensional (2D) problems with different longitudinal wavenumbers. A spectral finite element (SFEM) is proposed to represent waveguides in solids with arbitrary cross-section. Moreover, the BEM is extended to its spectral formulation (SBEM) to study unbounded fluid media and acoustic enclosures. Both approaches use Lagrange polynomials as element shape functions at the Legendre-Gauss-Lobatto (LGL) points. The fluid and solid subdomains are coupled by applying the appropriate boundary conditions at the limiting interface. The proposed method is verified by means of two benchmark problems: wave propagation in an unbounded acoustic medium and the scattering of waves by an elastic inclusion. The convergence and the computational effort are evaluated for different $h-p$ strategies. Numerical results show good agreement with the reference solution. Finally, the proposed method is used to study the pressure field generated by an array of elastic fluid-filled scatterers immersed in an acoustic medium.

Keywords: SBEM, SFEM, fluid-solid interaction, waveguide, scattered waves, two-and-a-half dimension

1. Introduction

Many engineering fields involve time harmonic wave propagation, such as fluid acoustics and solid scattering. Hybrid methods based on the boundary element method (BEM) and the finite element method (FEM) are suitable for studying solid and fluid interaction in unbounded media. Both methods have been used in various works to predict the response of coupled fluid-structure problems. For the low frequency range, the standard formulation using linear elements accurately represents the fluid and solid scattering

*Corresponding author
Email address: aro@us.es (A. Romero)

waves. However, at high frequencies, the solution deteriorates due to the so-called pollution effects [1, 2]. Higher-order approximations are needed to obtain accurate results.

Different approaches have been proposed in the past to overcome the pollution effect in two and three dimensional problems [3]. The h-refinement method has proved to be useless at high wavenumbers because of the necessary computational effort to represent small wavelengths [4]. Many works suggest using high-order elements to improve the convergence rate of standard formulations. The boundary and finite element methods have thus been extended to their spectral formulations [5, 6] approximating the field variables by high-order interpolation shape functions. Such functions are polynomials over non-uniformly spaced nodes to avoid the Runge phenomenon.

A number of authors have successfully applied spectral finite element methods in different fields. Degrande and De Roeck [7] developed a high-order formulation to study the dynamic response of a porous saturated medium using spectral elements. The authors used the analytical solution of Biot equations in two dimensions as shape functions. Bar-Yoseph et al. [8] proposed a spectral element method to study the transient response of a simply supported Euler-Bernoulli beam subjected to external forced lateral vibrations. They examined two Galerkin formulations using Hermitian and Lagrangian polynomials as interpolants for spatial and time discretisations. The space-time SFEM enabled the use of larger time steps while maintaining the accuracy of the solution. Kudela et al. [13] applied a SFEM to study the wave propagation in an isotropic rod and in a Timoshenko beam. The authors proposed this methodology to detect small damage in structures. The computed results were compared with those obtained from a standard FEM and from experimental measurements. This comparison highlighted the efficiency of the spectral elements. Zhu et al. [14] proposed the use of Chebyshev spectral elements within an implicit Newmark method to simulate acoustic wave propagation. They found accurate results with uniform nodal element distribution and small time steps. Recently, Romero et al. [17, 18] presented a spectral two-and-a-half dimensional (2.5D) formulation of two elements to study guided waves in coupled problems involving thin-walled structures and fluid-acoustic enclosures. They proposed a plate element based on a Reissner-Mindlin/Kirchhoff-Love mixed formulation to represent thin-walled structures. These authors found accurate results using an appropriate combination of element size and order of the approximation functions.

Regarding the development of the spectral boundary element method (SBEM), Calaon et al. [9] presented an approach to solve three dimensional (3D) elasticity problems using element shape functions generated from radial basis functions. They found that the exponential convergence of the solution was achievable. Holm et al. [10] extended the $hp-$version of the BEM to the Helmholtz equation to study the scattering of time harmonic acoustic waves at thin screens. Numerical experiments showed an exponential convergence rate and an arbitrarily high algebraic for the hp solution. Hwang [11] used a spectral approach to solve the boundary integral equation to study scattering and radiation problems. The spectral scheme presented orthogonal functions as basis functions to approximate the acoustic variables. Accurate results were found

with a reduction of computational effort with respect conventional BEM. Zou and Aliabadi [12] presented a boundary spectral element method for modelling high-frequency wave propagation in three dimensions. The authors used three types of high-order spectral elements for boundary discretisation. The computed results were validated against a well-stablished FEM. Milind and Mitra [15] studied time harmonic problems in acoustics using a Fourier-Hankel SBEM formulation. The authors compared the solution given by the SBEM with those obtained using the FEM, and other standard BEM techniques. Furthermore, Cerrato et al. [16] proposed a spectral coupled formulation of the BEM and the FEM to study linear water-wave propagation. They used the SFEM to study a closed region with non-constant bathymetry, and derived a SBEM from the mild-slope equation to study water-wave propagation over an infinite region with unidirectional variable bathymetry. They achieved very accurate results in comparison with the standard discrete solutions to this problem.

In this work, we propose a two-and-a-half dimensional coupled spectral formulation based on the FEM and the BEM to study wave propagation in fluid and solid waveguides. The proposed method is useful for problems whose geometry and material properties are both uniform in one direction, whereas the excitation exhibits a three dimensional distribution. The spectral approach allows the analysis of wave propagation at high wavenumbers, which reduces the pollution effect with low computational effort.

The outline of this work is as follows. First, the fluid-solid interaction problem is formulated in two-and-a-half dimensions. The 2.5D formulation of the BEM and the FEM are extended to their spectral formulations (SBEM and SFEM, respectively). The SBEM is used for the representation of both acoustic enclosures and unbounded domains. Moreover, a solid finite spectral element is proposed to represent elastic waveguides with arbitrary cross-section. The proposed approach is verified with two benchmark problems: the wave propagation in an unbounded acoustic region [16] and the scattering of waves by an elastic inclusion [19]. An $h-p$ convergence analysis is carried out to assess the accuracy of the method. Finally, the proposed method is applied to study the scattered wave field in an unbounded acoustic domain due to an array of elastic fluid-filled cylinders.

2. Numerical model

The spectral formulations of the BEM and FEM are developed to represent an elastic waveguide submerged in an unbounded acoustic region, as shown in Figure 1. The proposed methodology uses spectral solid elements to represent the elastic waveguide (Ω_s), while the limiting interface (Γ) between the solid and the fluid (Ω_f) is modelled with spectral boundary elements. Both methods are coupled by imposing the appropriate boundary conditions at the interface Γ: equilibrium of normal pressure and compatibility of normal displacement must be ensured at the fluid-solid interface, with null shear stresses. The governing

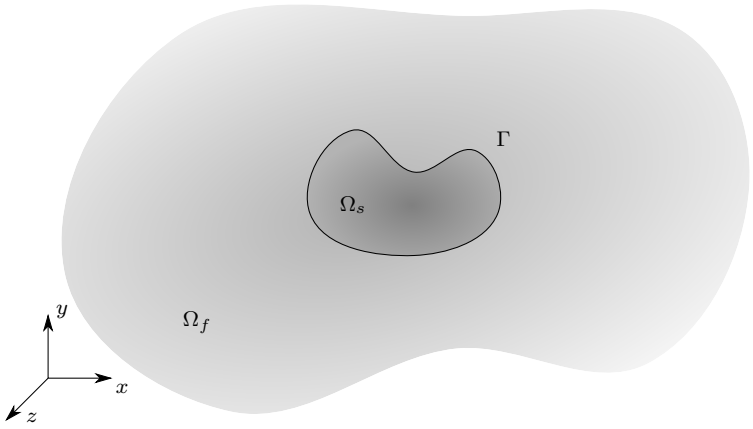

Figure 1: Domain decomposition

equations and the boundary conditions of the coupled fluid-solid system are:

$$\begin{cases} \nabla\boldsymbol{\sigma} + \mathbf{b} = \omega^2 \rho_s \mathbf{u}_s & \text{in } \Omega_s, \quad \text{with BC} \\ \nabla^2 p_f + \kappa_f^2 p_f = 0 & \text{in } \Omega_f, \quad \text{with BC} \\ \mathbf{u}_s^T \mathbf{n} = u_f & \text{in } \Gamma, \\ (\boldsymbol{\sigma}\mathbf{n})^T \mathbf{n} + p_f = 0 & \text{in } \Gamma, \end{cases} \tag{1}$$

where the variables in the solid equation are the stress tensor $\boldsymbol{\sigma}$, the body force vector $\mathbf{b}$, the displacement vector $\mathbf{u}_s$, the solid density ρ_s and the angular frequency ω. The Helmholtz equation defines the pressure field p_f for a fluid wavenumber $\kappa_f = \omega/c_f$, where c_f is the sound wave propagation velocity in the fluid subdomain. The coupling conditions include the fluid normal displacement to the boundary u_f and the outward solid normal at the interface Γ, $\mathbf{n}$.

The 2.5D formulation is handled by defining a characteristic field for the elastic and the acoustic waveguides at point $\mathbf{x} = \mathbf{x}(x, y, z)$ as [20, 21]:

$$\widehat{f}(\mathbf{x}, \kappa_z, \omega) = \widetilde{f}(\widetilde{\mathbf{x}}, \kappa_z, \omega)\, e^{-\iota \kappa_z z}, \tag{2}$$

where $\widetilde{f}(\widetilde{\mathbf{x}}, \kappa_z, \omega)$ is the frequency-wavenumber representation of an unknown variable (e.g. displacement, force or sound pressure), $\widetilde{\mathbf{x}} = \widetilde{\mathbf{x}}(x, y)$ and $\iota = \sqrt{-1}$. The 3D solution is computed as the superposition of 2D solutions with different wavenumber κ_z [22]:

$$f(\mathbf{x}, \omega) = \int_{-\infty}^{+\infty} \widetilde{f}(\widetilde{\mathbf{x}}, \kappa_z, \omega)\, e^{-\iota \kappa_z z} d\kappa_z. \tag{3}$$

The integral in Equation (3) presents poles and singularities, and the integration over the longitudinal wavenumber becomes mathematically and numerically complicated. One simple way around these difficulties is to replace the single-source problem, whose solution is expressed by Equation (3), with a multiple-source problem where sources are periodically distributed along the z axis [22]. Then, Equation (3) is replaced by:

$$f\left(\mathbf{x},\omega\right)=\int_{-\infty}^{+\infty}\widetilde{f}\left(\widetilde{\mathbf{x}},\kappa_z,\omega\right)e^{-\iota\kappa_z z}\sum_{m=-\infty}^{\infty}e^{\iota\kappa mL}d\kappa_z, \tag{4}$$

where L is the periodicity source interval. L needs to be large enough to avoid the response being contaminated by the virtual source. Then, Equation (4) reduces to:

$$f\left(\mathbf{x},\omega\right)=\frac{2\pi}{L}\sum_{n=-\infty}^{\infty}\widetilde{f}\left(\widetilde{\mathbf{x}},\kappa_{zn},\omega\right)e^{-\iota\kappa_{zn}z}d\kappa_z. \tag{5}$$

with $\kappa_{zn}=\frac{2\pi}{L}n$, which converges and can be approximated by a finite sum of N terms as:

$$f\left(\mathbf{x},\omega\right)=\frac{2\pi}{L}\sum_{n=-N}^{N}\widetilde{f}\left(\widetilde{\mathbf{x}},\kappa_{zn},\omega\right)e^{-\iota\kappa_{zn}z}d\kappa_z. \tag{6}$$

2.1. Spectral boundary element method (SBEM)

Next, the SBEM is derived from the standard collocation method, which is fully covered in the literature [23]. The main differences between the two methods concern the field variable approximation and the proposed element integration scheme. In both cases, the boundary integral representation is derived from the Helmholtz equation [23], considering a homogeneous fluid domain denoted by its volume Ω_f and its boundary Γ. Although the proposed method is used to obtain the three-dimensional radiated field by an elastic waveguide with an arbitrary cross section, the problem is computed as the superposition of 2D problems with different wavenumber κ_z. Therefore, the boundary Γ is reduced to its cross section Σ at the coordinate plane $z=0$. Thus, the integral representation of the fluid pressure for a point $\widetilde{\mathbf{x}}_i$ located at the boundary Γ in the frequency-wavenumber domain is:

$$c_i(\widetilde{\mathbf{x}}_i)\widetilde{p}_i(\widetilde{\mathbf{x}}_i,\kappa_z,\omega)=-\int_{\Sigma}\left(\iota\rho\omega^2\widetilde{u}_i(\widetilde{\mathbf{x}}_i,\kappa_z,\omega)\widetilde{\Psi}(\widetilde{\mathbf{x}},\kappa_z,\omega;\widetilde{\mathbf{x}}_i)+\widetilde{p}_i(\widetilde{\mathbf{x}}_i,\kappa_z,\omega)\frac{\partial\widetilde{\Psi}(\widetilde{\mathbf{x}},\kappa_z,\omega;\widetilde{\mathbf{x}}_i)}{\partial\mathbf{n}}\right)d\Sigma, \tag{7}$$

where $\widetilde{p}(\widetilde{\mathbf{x}}_i,\kappa_z,\omega)$ and $\widetilde{u}(\widetilde{\mathbf{x}}_i,\kappa_z,\omega)$ are the sound pressure and the particle normal displacement at the cross section Σ of the boundary Γ, respectively. $\widetilde{\Psi}(\widetilde{\mathbf{x}},\kappa_z,\omega;\widetilde{\mathbf{x}}_i)$ is the solution to the Helmholtz equation at point $\widetilde{\mathbf{x}}$ due to a point source located at $\widetilde{\mathbf{x}}_i$ [24]:

$$\widetilde{\Psi}(\widetilde{\mathbf{x}},\kappa_z,\omega;\widetilde{\mathbf{x}}_i)=-\frac{\iota}{4}H_0^{(2)}\left(k_\alpha r\right), \tag{8}$$

where $r=\|\widetilde{\mathbf{x}}-\widetilde{\mathbf{x}}_i\|$ is the distance to the source, $k_\alpha=\sqrt{k_f^2-\kappa_z^2}$ is the effective wavenumber and $H_0^{(2)}$ is the zero order Hankel function of second kind. The integral-free term $c_i(\widetilde{\mathbf{x}}_i)$ only depends on the boundary geometry at the collocation point $\widetilde{\mathbf{x}}_i$.

The solution to this integral is found by discretisation of the boundary into N element with $\Sigma=\bigcup_{j=1}^{N}\Sigma^j$:

$$c_i(\widetilde{\mathbf{x}}_i)\widetilde{p}_i(\widetilde{\mathbf{x}}_i,\kappa_z,\omega)=-\sum_{j=1}^{N}\left[\widetilde{h}_i^j\left(\widetilde{\mathbf{x}},\kappa_z,\omega;\widetilde{\mathbf{x}}_i\right)\widetilde{p}_j(\widetilde{\mathbf{x}}_j,\kappa_z,\omega)+\widetilde{g}_i^j\left(\widetilde{\mathbf{x}},\kappa_z,\omega;\widetilde{\mathbf{x}}_i\right)\widetilde{u}_j(\widetilde{\mathbf{x}}_j,\kappa_z,\omega)\right], \tag{9}$$

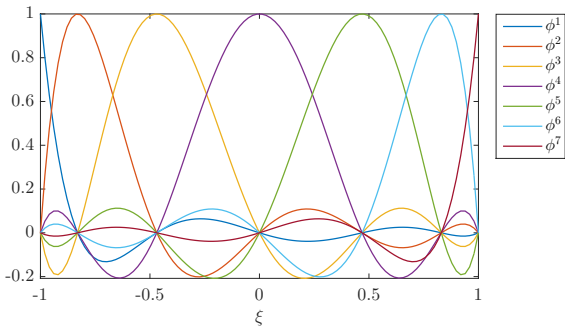

Figure 2: Element shape functions ϕ^k for an element with order $p = 6$.

where $\widetilde{g}_i^j$ and $\widetilde{h}_i^j$ are the boundary element matrices resulting from integration in element Σ^j and collocation at nodal point $\widetilde{\mathbf{x}}_i$. The field variables are approximated within the element using a set of interpolation shape functions $\phi(\xi)$ as:

$$\begin{aligned} \widetilde{p}_j(\widetilde{\mathbf{x}}_j, \kappa_z, \omega) &= \sum_{k=1}^{p+1} \phi^k \widetilde{p}(\widetilde{\mathbf{x}}_k, \kappa_z, \omega) = \boldsymbol{\phi}\widetilde{p}^e, \\ \widetilde{u}_j(\widetilde{\mathbf{x}}_j, \kappa_z, \omega) &= \sum_{k=1}^{p+1} \phi^k \widetilde{u}(\widetilde{\mathbf{x}}_k, \kappa_z, \omega) = \boldsymbol{\phi}\widetilde{u}^e. \end{aligned} \tag{10}$$

The proposed methodology uses Lagrange polynomials of order p as interpolation shape functions given by:

$$\phi^k = \prod_{j \neq i} \frac{\xi - \xi_i}{\xi_j - \xi_i}, \tag{11}$$

where nodal coordinates ξ_i are found at the Lobatto-Gauss-Legendre (LGL) points. The use of a family of orthogonal polynomial ($\phi^i(\xi_j) = \delta_{ij}$), such as Lagrange polynomials, as interpolation shape functions, mitigates the appearance of the Runge phenomenon, which can result in a highly ill-conditioned problem for high-order elements [25]. As an example, Figure 2 shows the shape functions for the element with order $p = 6$ used in this work.

Once the sound pressure and particle normal displacement are approximated within the element, the former integrals in Equation (9) become:

$$\widetilde{g}_i^j\left(\widetilde{\mathbf{x}}, \kappa_z, \omega; \widetilde{\mathbf{x}}_i\right) = \int_{\Sigma^j} \boldsymbol{\phi}\widetilde{\Psi}\left(\widetilde{\mathbf{x}}, \kappa_z, \omega; \widetilde{\mathbf{x}}_i\right) d\Sigma, \tag{12}$$

$$\widetilde{h}_i^j\left(\widetilde{\mathbf{x}}, \kappa_z, \omega; \widetilde{\mathbf{x}}_i\right) = \int_{\Sigma^j} \boldsymbol{\phi}\frac{\partial\widetilde{\Psi}\left(\widetilde{\mathbf{x}}, \kappa_z, \omega; \widetilde{\mathbf{x}}_i\right)}{\partial n} d\Sigma. \tag{13}$$

The spatial integrations in Equations (12) and (13) are numerically evaluated using a standard Gauss-Legendre quadrature with $(p + 1)$ integration points whenever the collocation point does not belong to

the integration element. However, the integrals become singular when the collocation point falls on the integration element. Then, the element integration is numerically evaluated by element subdivision, isolating the collocation point at the integration endpoints:

$$\begin{aligned}\int_{\Sigma^j} \widetilde{f}\left(\widetilde{\mathbf{x}}, \kappa_z, \omega; \widetilde{\mathbf{x}}_i\right) d\Sigma &= \int_{-1}^{1} \widetilde{f}\left(\widetilde{\mathbf{x}}, \kappa_z, \omega; \widetilde{\mathbf{x}}_i\right) |J^j(\xi)| d\xi \\ &= \int_{-1}^{\xi_p} \widetilde{f}\left(\widetilde{\mathbf{x}}, \kappa_z, \omega; \widetilde{\mathbf{x}}_i\right) |J^j(\xi)| d\xi + \int_{\xi_p}^{1} \widetilde{f}\left(\widetilde{\mathbf{x}}, \kappa_z, \omega; \widetilde{\mathbf{x}}_i\right) |J^j(\xi)| d\xi,\end{aligned} \tag{14}$$

with ξ_p being the natural coordinate of the collocation point $\widetilde{\mathbf{x}}_i$, $\widetilde{f}\left(\widetilde{\mathbf{x}}, \kappa_z, \omega; \widetilde{\mathbf{x}}_i\right)$ the kernel of integrals in Equations (12) and (13), and $|J^j(\xi)|$ the Jacobian of the transformation to the natural coordinate system for element Σ^j. A domain transformation is used for the treatment of the singular integrals as follows [26]:

$$\begin{cases} z_l^2 = \xi_p - \xi & , \quad -1 \leq \xi \leq \xi_p \\ z_r^2 = \xi - \xi_p & , \quad \xi_p \leq \xi \leq 1 \end{cases} \tag{15}$$

Then, integrals in Equation (14) can be rewritten as:

$$\int_{\Sigma} \widetilde{f}\left(\widetilde{\mathbf{x}}, k_z, \omega; \widetilde{\mathbf{x}}_i\right) d\Sigma = \int_{\sqrt{1+\xi_p}}^{0} \widetilde{f}\left(\widetilde{\mathbf{x}}, k_z, \omega; \widetilde{\mathbf{x}}_i\right) J(\xi) \frac{d\xi}{dz_l} dz_l + \int_{0}^{\sqrt{1-\xi_p}} \widetilde{f}\left(\widetilde{\mathbf{x}}, k_z, \omega; \widetilde{\mathbf{x}}_i\right) J(\xi) \frac{d\xi}{dz_r} dz_r \tag{16}$$

where $\frac{d\xi}{dz_l}$ and $\frac{d\xi}{dz_r}$ are respectively the Jacobian of the transformations obtained from Equation (15). The application of this polynomial transformation results in a significant improvement of convergence rates [26]. A linear transformation is used in order to transform the integration interval to $\eta \in [-1, 1]$:

$$\begin{cases} z_l = \frac{\sqrt{1+\xi_p}}{2}\left(1 + \eta_l\right) & , \quad -1 \leq \xi \leq \xi_p \\ z_r = \frac{\sqrt{1-\xi_p}}{2}\left(1 + \eta_r\right) & , \quad \xi_p \leq \xi \leq 1 \end{cases} \tag{17}$$

and Equation (16) becomes:

$$\int_{\Sigma} \widetilde{f}\left(\widetilde{\mathbf{x}}, k_z, \omega; \widetilde{\mathbf{x}}_i\right) d\Sigma = \int_{-1}^{1} \widetilde{f}\left(\widetilde{\mathbf{x}}, k_z, \omega; \widetilde{\mathbf{x}}_i\right) J(\xi) \frac{d\xi}{dz_l} \frac{dz_l}{d\eta_l} d\eta_l + \int_{-1}^{1} \widetilde{f}\left(\widetilde{\mathbf{x}}, k_z, \omega; \widetilde{\mathbf{x}}_i\right) J(\xi) \frac{d\xi}{dz_r} \frac{dz_r}{d\eta_r} d\eta_r \tag{18}$$

where $\frac{dz_l}{d\eta}$ and $\frac{dz_r}{d\eta}$ are the Jacobian of the linear transformations appliad by Equation (17). In this work, the integrals in Equation (18) are numerically evaluated using a Gauss-Legendre quadrature with $10(p+1)$ integration points. The integration scheme allowed accurate results as can be seen in the following section.

Finally, the boundary element matrices are assembled into a single system of equations relating sound pressure and particle normal displacement at nodal points:

$$\widetilde{\mathbf{H}}\left(\widetilde{\mathbf{x}}, \kappa_z, \omega\right) \widetilde{p}\left(\widetilde{\mathbf{x}}, \kappa_z, \omega\right) = \widetilde{\mathbf{G}}\left(\widetilde{\mathbf{x}}, \kappa_z, \omega\right) \widetilde{u}\left(\widetilde{\mathbf{x}}, \kappa_z, \omega\right), \tag{19}$$

where $\widetilde{p}\left(\widetilde{x}, \kappa_z, \omega\right)$ and $\widetilde{u}\left(\widetilde{\mathbf{x}}, \kappa_z, \omega\right)$ collect the nodal pressure and the normal displacement to the boundary, and $\widetilde{\mathbf{H}}\left(\widetilde{\mathbf{x}}, \kappa_z, \omega\right)$ and $\widetilde{\mathbf{G}}\left(\widetilde{\mathbf{x}}, \kappa_z, \omega\right)$ are the fully populated non-symmetrical boundary element system matrices.

Equation (19) can be modified in order to consider an incident pressure field to study scattering problems as:

$$\widetilde{\mathbf{H}}\left(\widetilde{\mathbf{x}},k_z,\omega\right)\widetilde{\mathbf{p}}\left(\widetilde{\mathbf{x}},k_z,\omega\right)=\widetilde{\mathbf{G}}\left(\widetilde{\mathbf{x}},k_z,\omega\right)\widetilde{\mathbf{u}}_n\left(\widetilde{\mathbf{x}},k_z,\omega\right)+\widetilde{\mathbf{p}}^I\left(\widetilde{\mathbf{x}},k_z,\omega\right), \tag{20}$$

where $\widetilde{\mathbf{p}}^I$ is an arbitrary incident pressure field. Once the boundary variables are solved, the radiated wave field at any receiver point in the fluid domain Γ_f is computed through the Somigliana identity. Then, the problem solution is defined as the superposition of the radiated wave field and the incident pressure field.

The assembled boundary element matrices require special treatment if the boundary has normal discontinuities. Since the sound pressure is unique at any point on the boundary, the element assembling into the matrix $\widetilde{\mathbf{H}}\left(\widetilde{\mathbf{x}},\kappa_z,\omega;\widetilde{\mathbf{x}}_i\right)$ is quite straightforward. However, the normal displacement at a discontinuity is not unique. This possibility is taken into account considering different values according to the element normals at this location. Nevertheless, the compatibility of normal displacements is not achieved when assembling matrix $\widetilde{\mathbf{G}}\left(\widetilde{\mathbf{x}},\kappa_z,\omega;\widetilde{\mathbf{x}}_i\right)$. Then, the assembled matrix has one extra column for each discontinuity point at the boundary and the normal displacement vector also has an extra component.

2.2. Spectral finite element method (SFEM)

The spectral finite element formulation is based on the virtual work principle in the frequency-wavenumber domain, which states [27]:

$$\begin{aligned}&-\omega^2\int_{\Omega_s}\delta\widehat{\mathbf{u}}^T(\mathbf{x},\kappa_z,\omega)\rho_s\widehat{\mathbf{u}}(\mathbf{x},\kappa_z,\omega)d\Omega+\int_{\Omega_s}\delta\widehat{\boldsymbol{\varepsilon}}^T(\mathbf{x},\kappa_z,\omega)\widehat{\boldsymbol{\sigma}}(\mathbf{x},\kappa_z,\omega)d\Omega\\&=\int_{\Omega_s}\delta\widehat{\mathbf{u}}^T(\mathbf{x},\kappa_z,\omega)\rho_s\widehat{\mathbf{b}}(\mathbf{x},\kappa_z,\omega)d\Omega+\int_{\Gamma}\delta\widehat{\mathbf{u}}^T(\mathbf{x},\kappa_z,\omega)\widehat{\mathbf{q}}(\mathbf{x},\kappa_z,\omega)d\Gamma,\end{aligned} \tag{21}$$

where $\widehat{\mathbf{u}}(\mathbf{x},\kappa_z,\omega)$ is the displacement vector, $\widehat{\boldsymbol{\varepsilon}}(\mathbf{x},\kappa_z,\omega)$ and $\widehat{\boldsymbol{\sigma}}(\mathbf{x},\kappa_z,\omega)$ are respectively the strain and stress tensors, $\rho_s\widehat{\mathbf{b}}(\mathbf{x},\kappa_z,\omega)$ is the body force in the domain Ω_s, ρ_s is the solid density, and $\widehat{\mathbf{q}}(\mathbf{x},\kappa_z,\omega)$ is the surface force vector. A variable preceded by δ denotes a compatible variation of the displacement or the strain field. Voigh notation is used to write both the symmetrical stress tensor $\widehat{\boldsymbol{\sigma}}$ and the strain tensor $\widehat{\boldsymbol{\varepsilon}}$, $\widehat{\boldsymbol{\sigma}}=\{\widehat{\sigma}_{xx},\widehat{\sigma}_{yy},\widehat{\sigma}_{zz},\widehat{\sigma}_{xy},\widehat{\sigma}_{yz},\widehat{\sigma}_{zx}\}^T$ and $\widehat{\boldsymbol{\varepsilon}}=\{\widehat{\varepsilon}_{xx},\widehat{\varepsilon}_{yy},\widehat{\varepsilon}_{zz},\widehat{\gamma}_{xy},\widehat{\gamma}_{yz},\widehat{\gamma}_{zx}\}^T$, respectively.

The stress tensor is related to the strain tensor through the constitutive relation:

$$\widehat{\boldsymbol{\sigma}}=\mathbf{C}\widehat{\boldsymbol{\varepsilon}}, \tag{22}$$

where, in the case of a linear isotropic material, the constitutive matrix $\mathbf{C}$ depends on the Young's modulus

E and the Poisson ratio ν:

$$\mathbf{C} = \frac{E}{(1+\nu)(1-2\nu)} \begin{bmatrix} 1-\nu & \nu & \nu & 0 & 0 & 0 \\ \nu & 1-\nu & \nu & 0 & 0 & 0 \\ \nu & \nu & 1-\nu & 0 & 0 & 0 \\ 0 & 0 & 0 & \frac{1-2\nu}{2} & 0 & 0 \\ 0 & 0 & 0 & 0 & \frac{1-2\nu}{2} & 0 \\ 0 & 0 & 0 & 0 & 0 & \frac{1-2\nu}{2} \end{bmatrix}. \tag{23}$$

The strain tensor can be derived from the displacement vector $\widehat{\mathbf{u}}$ as:

$$\widehat{\boldsymbol{\varepsilon}} = \mathbf{L}\widehat{\mathbf{u}}, \tag{24}$$

where:

$$\mathbf{L} = \begin{bmatrix} \frac{\partial}{\partial x} & 0 & 0 \\ 0 & \frac{\partial}{\partial y} & 0 \\ 0 & 0 & 0 \\ \frac{\partial}{\partial y} & \frac{\partial}{\partial x} & 0 \\ 0 & \frac{\partial}{\partial z} & \frac{\partial}{\partial y} \\ \frac{\partial}{\partial z} & 0 & \frac{\partial}{\partial x} \end{bmatrix}. \tag{25}$$

The dependence of the strain tensor on the longitudinal coordinate z can be removed considering the displacement definition in the frequency-wavenumber domain according to Equation (2):

$$\widehat{\mathbf{u}}\left(\mathbf{x}, \kappa_z, \omega\right) = \widetilde{\mathbf{u}}\left(\widetilde{\mathbf{x}}, \kappa_z, \omega\right) e^{-\iota\kappa_z z}. \tag{26}$$

Then, Equation (24) can be rewritten as:

$$\widehat{\boldsymbol{\varepsilon}} = \mathbf{L}_1\widehat{\mathbf{u}} + \mathbf{L}_2\frac{\partial\widehat{\mathbf{u}}}{\partial z} = \mathbf{L}_1\widehat{\mathbf{u}} - \iota\kappa_z\mathbf{L}_2\widehat{\mathbf{u}}, \tag{27}$$

where the differential operators are:

$$\mathbf{L}_1 = \begin{bmatrix} \frac{\partial}{\partial x} & 0 & 0 \\ 0 & \frac{\partial}{\partial y} & 0 \\ 0 & 0 & 0 \\ \frac{\partial}{\partial y} & \frac{\partial}{\partial x} & 0 \\ 0 & 0 & \frac{\partial}{\partial y} \\ 0 & 0 & \frac{\partial}{\partial x} \end{bmatrix}, \qquad \mathbf{L}_2 = \begin{bmatrix} 0 & 0 & 0 \\ 0 & 0 & 0 \\ 0 & 0 & 1 \\ 0 & 0 & 0 \\ 0 & 1 & 0 \\ 1 & 0 & 0 \end{bmatrix}. \tag{28}$$

The 2.5D formulation is derived assuming, as in the previous section, that solid material properties and geometry are both homogeneous in the longitudinal direction. Therefore, Equation (21) is further elaborated

by rewriting the volume integrals over the longitudinal coordinate z, and over the cross section A_s of the domain integration Ω_s with the coordinate plane $z = 0$:

$$\begin{aligned} &-\omega^2 \int_{-\infty}^{\infty} \left[\int_{A_s} \delta\widetilde{\mathbf{u}}^T \rho_s \widetilde{\mathbf{u}} dA \right] e^{-\iota\kappa_z z} dz + \int_{-\infty}^{\infty} \left[\int_{A_s} \delta\widetilde{\boldsymbol{\varepsilon}}^T \widetilde{\boldsymbol{\sigma}} dA \right] e^{-\iota\kappa_z z} dz \\ &= \int_{-\infty}^{\infty} \left[\int_{A_s} \delta\widetilde{\mathbf{u}}^T \rho_s \widetilde{\mathbf{b}} dA \right] e^{-\iota\kappa_z z} dz + \int_{-\infty}^{\infty} \left[\int_{\Sigma} \delta\widetilde{\mathbf{u}}^T \widetilde{\mathbf{q}} d\Sigma \right] e^{-\iota\kappa_z z} dz, \end{aligned} \tag{29}$$

where Σ is defined from the boundary Γ at $z = 0$. Then, Equation (29) must be fulfilled if:

$$-\omega^2 \int_{A_s} \delta\widetilde{\mathbf{u}}^T \rho_s \widetilde{\mathbf{u}} dA + \int_{A_s} \delta\widetilde{\boldsymbol{\varepsilon}}^T \widetilde{\boldsymbol{\sigma}} dA = \int_{A_s} \delta\widetilde{\mathbf{u}}^T \rho_s \widetilde{\mathbf{b}} dA + \int_{\Sigma} \delta\widetilde{\mathbf{u}}^T \widetilde{\mathbf{q}} d\Sigma. \tag{30}$$

The solid subdomain is discretised into elements, where the approximated displacement vector $\widetilde{\mathbf{u}}$ is defined as:

$$\widetilde{\mathbf{u}} = \boldsymbol{\varphi}\widetilde{\mathbf{u}}^e, \tag{31}$$

where $\boldsymbol{\varphi}$ are the two-dimensional shape functions obtained from the one-dimensional function $\phi(\xi)$ as:

$$\varphi^k(\xi, \eta) = \phi^i(\xi)\phi^j(\eta)\,, \qquad k = (i-1)(p+1) + j. \tag{32}$$

Then, Equation (31) can be rewritten as:

$$\widetilde{\mathbf{u}} = \sum_{i=1}^{p+1} \sum_{j=1}^{p+1} \left(\phi^i(\xi)\phi^j(\eta) \right) \widetilde{\mathbf{u}}(\xi_i, \eta_j) = \sum_{k=1}^{(p+1)^2} \varphi^k(\xi, \eta)\widetilde{\mathbf{u}}^k. \tag{33}$$

The proposed spectral finite element is defined from local nodal coordinates $(\xi, \eta) \in ([-1, 1] \times [-1, 1])$ at the LGL points. As an example, Figure 3 shows the natural coordinate system for an element of order $p = 6$, and its related element shape function φ^{25}.

Once the element approximation is defined, the strain tensor is expressed from the nodal displacement as:

$$\widetilde{\boldsymbol{\varepsilon}}^e = \mathbf{L}_1\boldsymbol{\varphi}\widetilde{\mathbf{u}}^e - \iota\kappa_z\mathbf{L}_2\boldsymbol{\varphi}\widetilde{\mathbf{u}}^e = \mathbf{B}_1\widetilde{\mathbf{u}}^e - \iota\kappa_z\mathbf{B}_2\widetilde{\mathbf{u}}^e, \tag{34}$$

where $\mathbf{B}_1 = \mathbf{L}_1\boldsymbol{\varphi}$ and $\mathbf{B}_2 = \mathbf{L}_2\boldsymbol{\varphi}$.

Introducing Equations (22), (31) and (34) into Equation (30), the virtual work principle can be rewritten for each element as:

$$\begin{aligned} &-\omega^2 \int_{A_s^e} \delta\widetilde{\mathbf{u}}^{eT} \boldsymbol{\varphi}^T \rho_s \boldsymbol{\varphi} \widetilde{\mathbf{u}}^e dA + \int_{A_s^e} \left(\delta\widetilde{\mathbf{u}}^{eT} \mathbf{B}_1^T - \iota\kappa_z \delta\widetilde{\mathbf{u}}^{eT} \mathbf{B}_2^T \right) \mathbf{C} \left(\mathbf{B}_1\widetilde{\mathbf{u}}^e - \iota\kappa_z \mathbf{B}_2\widetilde{\mathbf{u}}^e \right) dA \\ &= \int_{A_s^e} \delta\widetilde{\mathbf{u}}^{eT} \boldsymbol{\varphi}^T \rho_s \widetilde{\mathbf{b}}^e dA + \int_{\Sigma^e} \delta\widetilde{\mathbf{u}}^{eT} \boldsymbol{\varphi}^T \widetilde{\mathbf{q}}^e d\Sigma, \end{aligned} \tag{35}$$

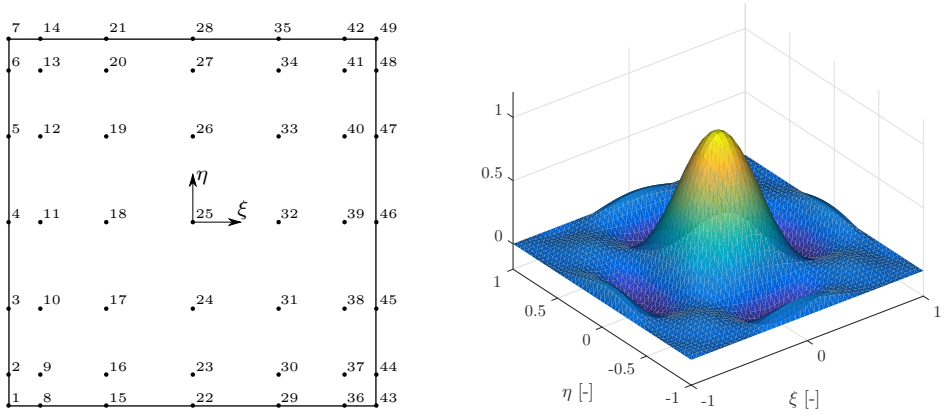

(a) (b)

Figure 3: (a) Element natural coordinate system and (b) element shape function φ^{25} for an element of order $p = 6$.

where A_s^e is the cross-sectional area of the three dimensional element in the z direction and Σ^e its boundary. This equation is further elaborated by operating on the second integral of the left-hand side:

$$\begin{aligned} &-\omega^2 \int_{A_s^e} \delta\widetilde{\mathbf{u}}^{eT} \boldsymbol{\varphi}^T \rho_s \boldsymbol{\varphi} \widetilde{\mathbf{u}}^e dA + \int_{A_s^e} \delta\widetilde{\mathbf{u}}^{eT} \mathbf{B}_1^T \mathbf{C} \mathbf{B}_1 \widetilde{\mathbf{u}}^e dA \\ &-\iota\kappa_z \int_{A_s^e} \delta\widetilde{\mathbf{u}}^{eT} \left(\mathbf{B}_1^T \mathbf{C} \mathbf{B}_2 + \mathbf{B}_2^T \mathbf{C} \mathbf{B}_1 \right) \widetilde{\mathbf{u}}^e dA - \kappa_z^2 \int_{A_s^e} \delta\widetilde{\mathbf{u}}^{eT} \mathbf{B}_2^T \mathbf{C} \mathbf{B}_2 \widetilde{\mathbf{u}}^e dA \\ &= \int_{A_s^e} \delta\widetilde{\mathbf{u}}^{eT} \boldsymbol{\varphi}^T \rho_s \widetilde{\mathbf{b}}^e dA + \int_{\Sigma^e} \delta\widetilde{\mathbf{u}}^{eT} \boldsymbol{\varphi}^T \widetilde{\mathbf{q}}^e d\Sigma. \end{aligned} \tag{36}$$

The following expression is obtained taking into account that Equation (36) must be satisfied for any compatible displacement $\delta\widetilde{\mathbf{u}}^e$:

$$\left[-\omega^2 \mathbf{M}^e + \mathbf{K}_0^e - \iota\kappa_z \mathbf{K}_1^e - \kappa_z^2 \mathbf{K}_2^e \right] \widetilde{\mathbf{u}}^e = \widetilde{\mathbf{f}}^e, \tag{37}$$

where $\mathbf{M}^e$ is the element mass matrix, $\mathbf{K}_0^e$, $\mathbf{K}_1^e$ and $\mathbf{K}_2^e$ are the element stiffness matrices and $\widetilde{\mathbf{f}}^e$ is a vector that collects the forces applied to the element. These matrices are defined by:

$$\mathbf{M}^e = \int_{A_s^e} \boldsymbol{\varphi}^T \rho_s \boldsymbol{\varphi} dA, \tag{38}$$

$$\mathbf{K}_0^e = \int_{A_s^e} \mathbf{B}_1^T \mathbf{C} \mathbf{B}_1 dA, \tag{39}$$

$$\mathbf{K}_1^e = \int_{A_s^e} \left(\mathbf{B}_1^T \mathbf{C} \mathbf{B}_2 - \mathbf{B}_2^T \mathbf{C} \mathbf{B}_1 \right) dA, \tag{40}$$

$$\mathbf{K}_2^e = \int_{A_s^e} \mathbf{B}_2^T \mathbf{C} \mathbf{B}_2 dA, \tag{41}$$

and the external load vector $\widetilde{\mathbf{f}}^e$ as:

$$\widetilde{\mathbf{f}}^e\left(\widetilde{\mathbf{x}},\kappa_z,\omega\right)=\int_{A_s^e}\boldsymbol{\varphi}^T\rho_s\widetilde{\mathbf{b}}^e(\widetilde{\mathbf{x}},\kappa_z,\omega)dA+\int_{\Sigma^e}\boldsymbol{\varphi}^T\widetilde{\mathbf{q}}^e(\widetilde{\mathbf{x}},\kappa_z,\omega)d\Sigma, \tag{42}$$

which contains the contributions of both body forces and surface loads.

Then, Equation (37) can be written as:

$$\widetilde{\mathbf{K}}\widetilde{\mathbf{u}}=\widetilde{\mathbf{f}}, \tag{43}$$

where $\widetilde{\mathbf{K}}=[-\omega^2\mathbf{M}+\mathbf{K}_0-\iota\kappa_z\mathbf{K}_1-\kappa_z^2\mathbf{K}_2]$ is the dynamic stiffness matrix obtained in the frequency-wavenumber domain from the assembled mass $\mathbf{M}$ matrix, and stiffness $\mathbf{K}_0$, $\mathbf{K}_1$ and $\mathbf{K}_2$ matrices.

The mass $\mathbf{M}^e$ matrix and stiffness $\mathbf{K}_0^e$, $\mathbf{K}_1^e$ and $\mathbf{K}_2^e$ matrices are numerically integrated using a LGL quadrature of order $p+1$. Therefore, the nodal element coordinates coincide with the element integration points producing a diagonal mass $\mathbf{M}^e$ matrix and stiffness $\mathbf{K}_2^e$ matrices, that can be easily computed as follows:

$$\begin{aligned}
\mathbf{M}^e_{kl} =&\delta_{kl}\rho w_{ij}\left|\mathbf{J}_{ij}\right|,\\
\mathbf{K}^e_{2\,kl} =&\delta_{kl}\frac{E}{(1+\nu)(1-2\nu)}\gamma_m w_{ij}\left|\mathbf{J}_{ij}\right|,\\
&\text{with } i,j=1,...,p+1,\\
&\text{and } k=3\left[(i-1)(p+1)+(j-1)\right]+m,\\
&\text{and } l=3\left[(i-1)(p+1)+(j-1)\right]+n,\ m,n=1,2,3,\\
&\gamma_m=\begin{cases}\frac{1-2\nu}{\nu} & \text{for}\quad m=1,2,\\ 1-\nu & \text{for}\quad m=3,\end{cases}
\end{aligned} \tag{44}$$

where w_{ij} is the integration weight at (ξ_i,η_j), and $|\mathbf{J}_{ij}|$ is the Jacobian evaluated at (ξ_i,η_j).

2.3. SBEM-SFEM coupling

Equations (19) and (43) are coupled by imposing equilibrium of forces, compatibility of normal displacement and null shear stresses at the interface Γ. These equations are assembled into a single comprehensive system, together with the equilibrium and compatibility conditions.

The load vector $\widetilde{\mathbf{f}}_f$ at the fluid-solid interface is obtained by integrating the fluid pressure field $\widetilde{p}_f$ over the boundary Γ:

$$\widetilde{\mathbf{f}}_f=-\int_\Gamma\boldsymbol{\varphi}^T\mathbf{n}\boldsymbol{\phi}\widetilde{p}_f d\Gamma=-\mathbf{R}^T\widetilde{p}_f, \tag{45}$$

where $\mathbf{n}$ is the outward normal vector at Γ, and $\mathbf{R}$ is the coupling fluid-solid matrix which relates force at the solid subdomain and pressure at the boundary. Once the pressure has been integrated over the boundary, the force vector defined by Equation (42) can be split according to the subdomain definition (Figure 1) and

equilibrium of forces can be applied. Then, substituting Equation (45) into Equation (43) yields:

$$\begin{bmatrix} \widetilde{\mathbf{K}}_{ss} & \widetilde{\mathbf{K}}_{sf} \\ \widetilde{\mathbf{K}}_{fs} & \widetilde{\mathbf{K}}_{ff} \end{bmatrix} \begin{bmatrix} \widetilde{\mathbf{u}}_s \\ \widetilde{\mathbf{u}}_f \end{bmatrix} = \begin{bmatrix} \widetilde{\mathbf{f}}_s \\ -\mathbf{R}^T \widetilde{p}_f \end{bmatrix}, \tag{46}$$

where the subscript f indicates degrees of freedom belonging to Γ and s stands for the rest of solid degrees of freedom.

Finally, the coupling of Equations (19) and (46) is carried out with the imposition of compatibility of normal displacement at the boundary Γ, and null shear-stresses. Both systems of equations are assembled into an overall system:

$$\begin{bmatrix} \widetilde{\mathbf{K}}_{ss} & \widetilde{\mathbf{K}}_{sf} & \mathbf{0} \\ \widetilde{\mathbf{K}}_{fs} & \widetilde{\mathbf{K}}_{ff} & \mathbf{R}^T \\ \mathbf{0} & -\widetilde{\mathbf{G}}\mathbf{N}^T & \widetilde{\mathbf{H}} \end{bmatrix} \begin{bmatrix} \widetilde{\mathbf{u}}_s \\ \widetilde{\mathbf{u}}_f \\ \widetilde{p}_f \end{bmatrix} = \begin{bmatrix} \widetilde{\mathbf{f}}_s \\ \widetilde{\mathbf{f}}_f \\ \mathbf{0} \end{bmatrix}, \tag{47}$$

where $\mathbf{N}$ is a matrix containing the outward normal vector $\mathbf{n}$ at the boundary. Equation (47) is solved for each frequency-wavenumber step to compute the coupled fluid-solid response.

3. Model verification

The proposed SBEM-SFEM formulation was verified with two benchmark problems on the propagation of acoustic waves over an unbounded fluid domain [16], and the wave scattering by a cylindrical elastic waveguide [19].

Different $h-p$ strategies were investigated to get accurate discretisation with low computational effort. The nodal density per wavelength is used to describe the mesh density:

$$d_\lambda = \frac{2\pi p}{h\kappa^*}, \tag{48}$$

where κ^* is a characteristic wavenumber of the studied domain, h is the element length and p is the element order. Two different $h-p$ convergence analyses were carried out for three different discretisation at each case with successive $p-$enrichment. Starting from a coarse mesh, the elements were subdivided in order to perform a h-refinement, and the element order was increased until numerical results converged.

3.1. Wave propagation over an unbounded acoustic medium

This section analyses the accuracy of the proposed SBEM with a benchmark problem regarding wave propagation in an unbounded domain. An artificial open boundary was modelled with essential boundary conditions defined at $x = 0$ m and $x = 2$ m and Neumann conditions at $y = 0$ m and $y = 1$ m (Figure 4). An incident pressure field given by $\widetilde{p}^I = e^{\iota\kappa_f \widetilde{\mathbf{d}}\cdot\widetilde{\mathbf{x}}}$ was considered, with a polarised direction $\widetilde{\mathbf{d}} = \{\cos\pi/6, \sin\pi/6\}^T$. This problem has an analytical solution for the two-dimensional Helmholtz equation that is equivalent to setting the longitudinal wavenumber at $\kappa_z = 0$ rad/m.

The problem solution was computed for a fluid wavenumber $\kappa_f = 15$ rad/m, assuming a sound wave propagation velocity $c_f = 1500$ rad/m and fluid density $\rho_f = 1000$ kg/m^3. This problem was also studied by Cerrato et al. [16] in the development of an SBEM to study water-wave propagation. The accuracy of the proposed method was assessed through the L_∞-error norm for approximating the analytical solution given by the incident wave field. Moreover, computed results were also compared with those in Reference [16].

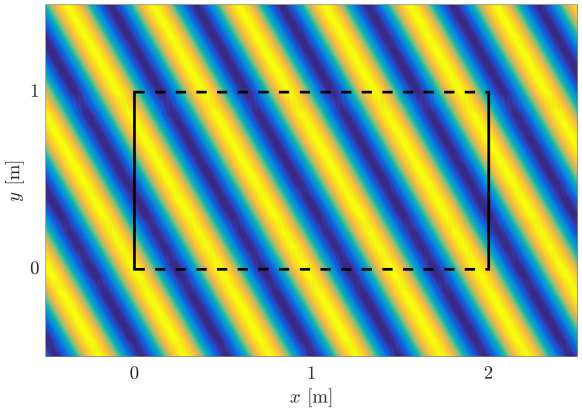

Figure 4: Wave propagation over an unbounded domain. Dirichlet (solid lines) and Neumann (dashed lines) boundary conditions.

Three different meshes were investigated to study the convergence of the proposed method, resulting in a characteristic element length given by $1/h = \{3, 5, 15\}$ m^{-1}. The element order was successively increased until reaching the convergence for each discretisation. The analysis was limited to quadratic and high order elements. Constant and linear elements did not produce accurate results due to the interpolation error, especially in coarse meshes.

Figure 5(a) shows the L_∞-error for different discretisations h and element order p. The error curves show an exponential decay from $p = 2$ until the convergence was reached for an error of $\mathcal{O}(10^{-6})$. The error decay rate was higher for finer discretisations and the solution convergence was faster than in coarser meshes. Computed results were quite similar to those presented in Reference [16] for the error range above $\mathcal{O}(10^{-6})$. Cerrato et. al [16] achieved more accurate results by increasing the element order using an analytical integration of singular kernels. However, adopting a numerical integration scheme can be useful for the development of the SBEM due to its simplicity.

Figure 5(b) relates the L_∞-error with the CPU time, finding a nearly linear rate with a slope between -12:1 and -15:1 in the double logarithmic scale. Moreover, finer discretisations achieved lower errors for a

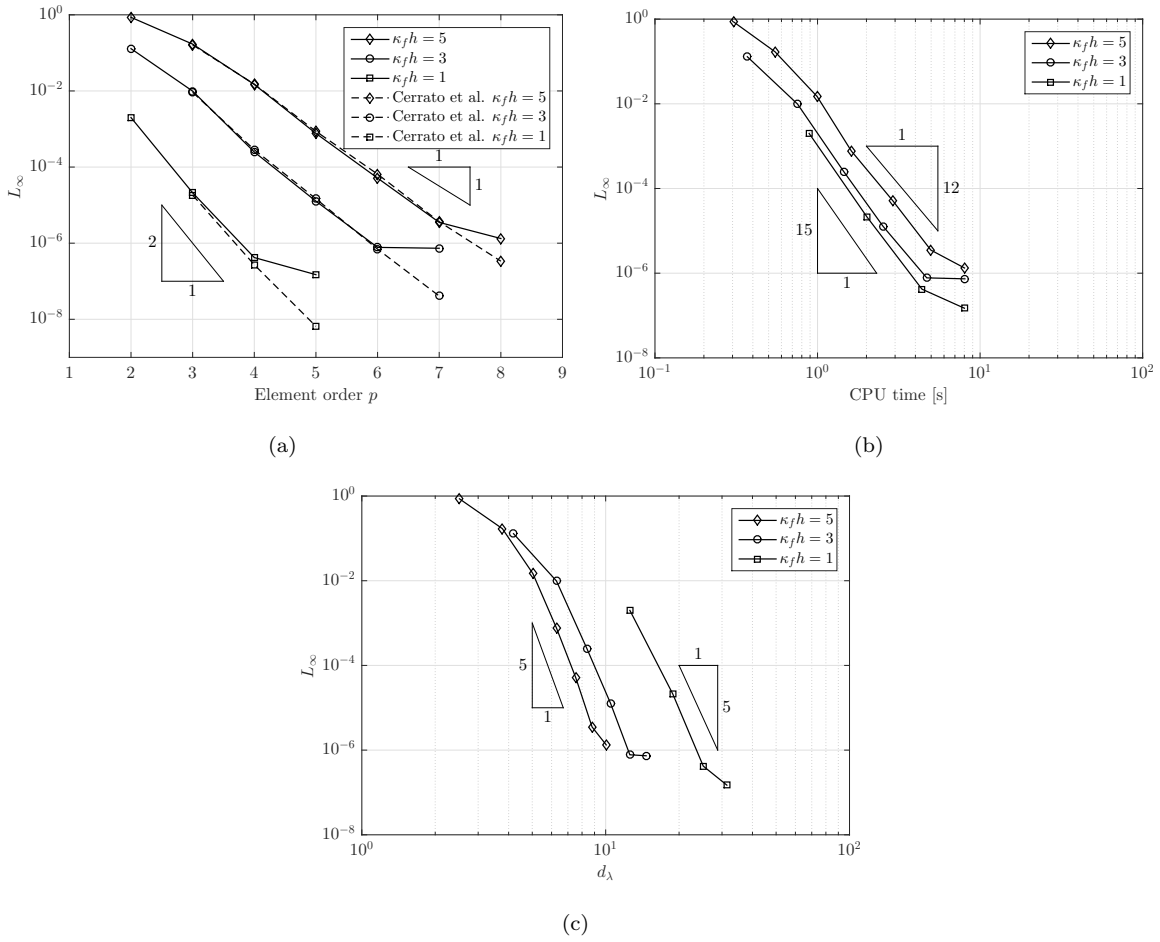

Figure 5: L_∞-error representation over: (a) element order, (b) CPU time and (c) nodal density per wavelength.

given CPU time, but needed higher nodal densities per wavelength which is related to the memory usage (Figure 5(c)). The CPU time depends on the total element integrations and the number of collocation points. For a given mesh with n_{elem} boundary elements and $n_{elem}(p+1)$ collocation points results in $[n_{elem}(p+1)]^2$ operations, when a quadrature rule of $p+1$ points is used. We found that element integrations involved the computation of the fundamental solution and the evaluation of the shape functions, that mainly depended on the element order. Then, the total CPU time was of form $C(p)\,[n_{elem}(p+1)]^2$. The computational cost had a higher dependency on the element order approximation than on the discretisation size. This fact indicated that a combined *hp*-refinement is desirable to reduce the computational effort. Problem discretisation with nodal densities around $d_\lambda = 10$ and $\kappa_f h = 3$ gave a good approximation, reducing the computational effort in terms of CPU time and memory requirements.

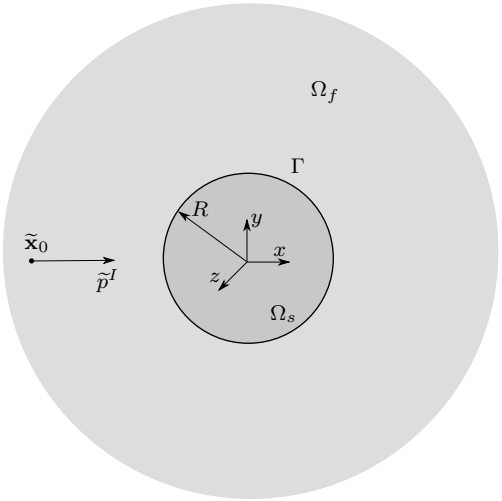

Figure 6: Elastic inclusion in an unbounded acoustic region

3.2. Wave scattering by a cylindrical elastic waveguide

The proposed coupled spectral boundary and finite element method was verified from a benchmark problem involving a cylindrical elastic waveguide in a homogeneous unbounded fluid medium. The inclusion had a radius $r = 0.6$ m. The solid properties were compression wave propagation velocity $c_p = 2630$ m/s, shear wave propagation velocity $c_s = 1416$ m/s, and density $\rho_s = 2250$ kg/m^3, while the fluid properties were sound wave propagation velocity $c_f = 1500$ m/s and density $\rho_f = 1000$ kg/m^3. The proposed SFEM represented the solid inclusion, while the SBEM was used to model the fluid domain.

The elastic inclusion was subjected to a dilatational point source located in the fluid at $\widetilde{\mathbf{x}}_0 = (-3.5, 0)$ from the cavity centre (Figure 6). The incident wave field $\widetilde{p}^I(\widetilde{\mathbf{x}}, \kappa_z, \omega)$ was defined from the fundamental solution $\widetilde{\Psi}(\widetilde{\mathbf{x}}, \kappa_z, \omega)$ [24] as:

$$\widetilde{p}^I(\widetilde{\mathbf{x}}, \kappa_z, \omega) = 2\widetilde{\Psi}(\widetilde{\mathbf{x}}, \kappa_z, \omega). \tag{49}$$

The problem solution was computed for a fluid wavenumber $\kappa_f = 5.236$ rad/m. A constant value of $\kappa_z = 1.0$ rad/m was assumed for comparison purposes. The analytical solution to this problem can be found in Reference [19]. The numerical results were compared with the reference solution and the scaled L_2-error ϵ_2 was used to asses the accuracy of the proposed method.

Figure 7 represents the real part of the analytical solution of the fluid pressure around the inclusion, and the horizontal and longitudinal solid displacements. Maximum amplitudes of the pressure are found near the source, because of the superposition of the incident and the scattered pressure fields, and behind the inclusion, due to the propagation of the incident wave through it. Both the pressure and the displacements present symmetry with respect the horizontal axis.

Three discretisations were investigated. The characteristic element sizes were $1/h = \{2.12, 4.24, 8.48\}$ m^{-1}, resulting in $\kappa_f h = \{2.47, 1.23, 0.62\}$. The element order p was set to obtain nodal densities per wavelength $d_\lambda = \{5, 7.5, 10, 15, 20\}$, which was limited to $d_\lambda = 20$ for the finest discretisation because of the element size. Figure 8 shows a coarse, a medium and a fine problem discretisation that ensure $d_\lambda = 20$.

Table 1 summarizes the computed scaled L_2-error ϵ_2 and the CPU time for the different $h-p$ discretisations used in this problem. The computed results presented a good agreement with the reference solution,

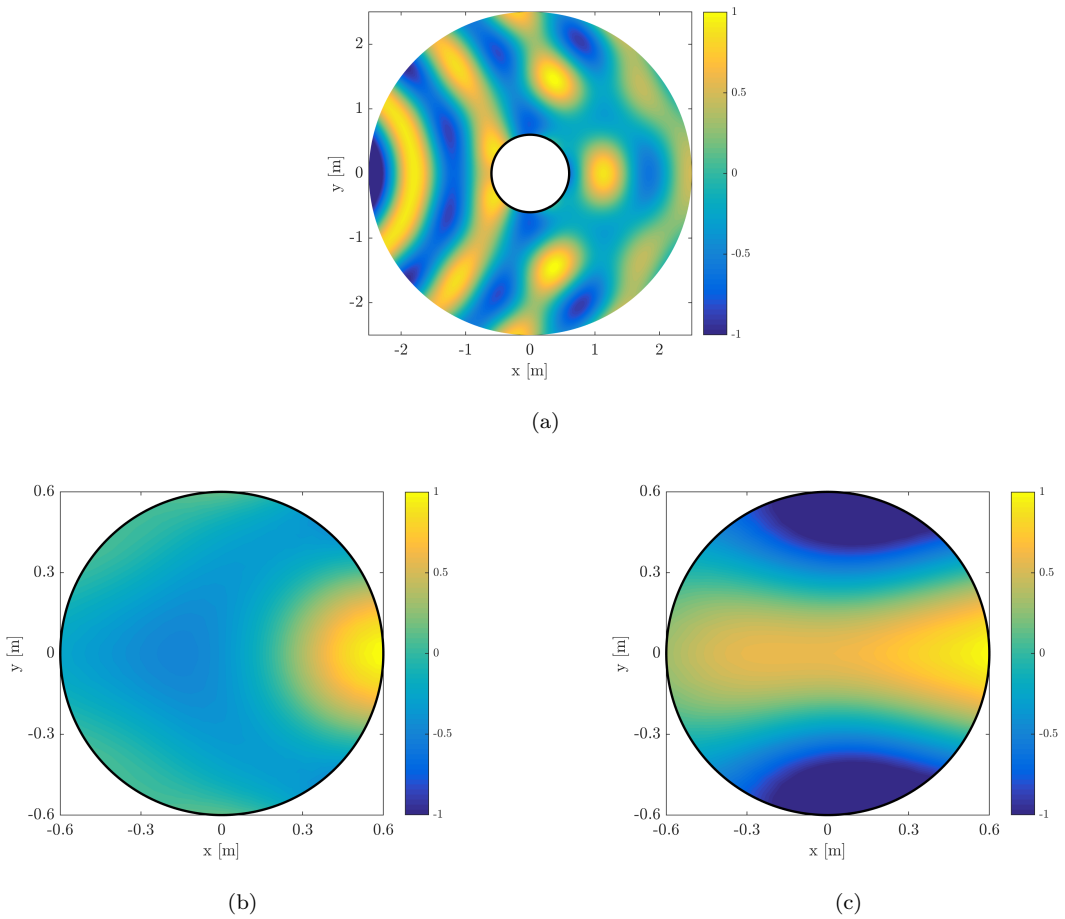

Figure 7: Real part of the analytical solution for (a) total fluid pressure, (b) horizontal solid displacement and (c) longitudinal solid displacement. $k_f = 5.236\,\mathrm{rad/m}$ and $k_z = 1.0\,\mathrm{rad/m}$

as the error varied from $\epsilon_2 \approx 1 \times 10^{-3}$ to $\epsilon_2 \approx 1 \times 10^{-5}$. However, the coarsest mesh did not accurately represent the problem solution for low element orders, since the nodal density per wavelength was not high enough. The smallest error was found for the medium size discretisation with an acceptable computational time, while the finest mesh had a higher error in a lower time. On the other hand, the coarsest mesh needed a higher computational effort to reach a similar level of error because of the higher element order approximation. Furthermore, the coarsest mesh presented an error decay up to an element order of $p = 6$, where the convergence was truncated. This behaviour comes from the integration of singularities in Equations (12) and (13). Then, the accuracy of the coupled method is limited by the accuracy of the SBEM.

As previously commented, the CPU time in the SBEM depends on the element order and problem discretisation. Similarly, in the case of the SFEM, the necessary number of operations to do the element integrations was $n_{elem}(p+1)^2$ for a given mesh with n_{elem} elements. The CPU time of the SFEM was proportional to the total number of operations depending on the element order by $C'(p)$. Then, the CPU

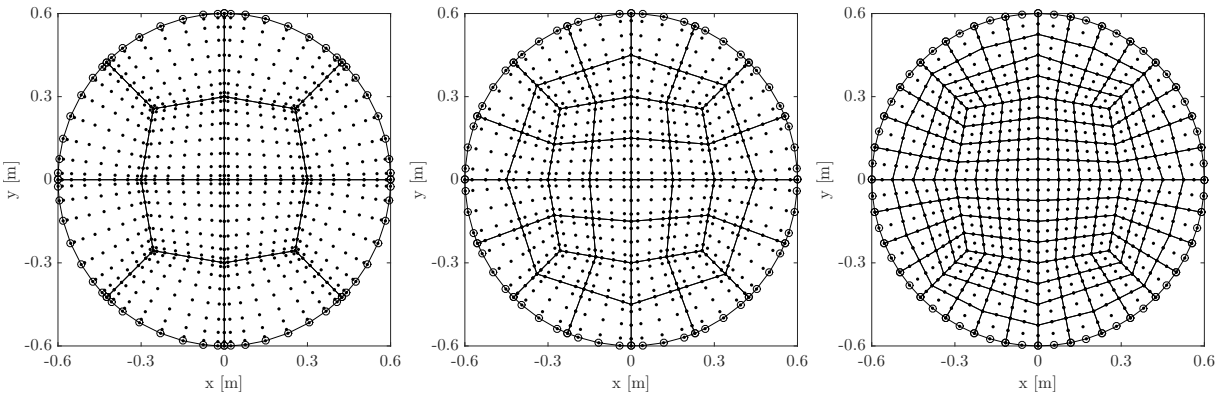

(a) (b) (c)

Figure 8: Problem discretisation using (a) coarse, (b) medium, and (c) fine meshes with nodal density $d_\lambda = 20$. SBEM nodes are represented by circles and SFEM nodes by points

time can be described as $C'(p)n_{elem}(p+1)^2$. Moreover, the computational cost of the SFEM was much more lower than the SBEM while, in comparison, the CPU time of coupling and solving the system of equations was practically negligible. Again, a *hp*-refinement is more efficient in terms of error and computational effort than a single *h*-refinement or *p*-refinement.

4. Numerical example

Finally, the capabilities of the proposed method are explored with a numerical example. The problem solved herein was the study of the scattered wave field by an array of elastic cylinders submerged in an inviscid fluid medium (Figure 9). The elastic cylinders had an external radius $r = 0.4$ m and a thickness $t = 0.05$ m. The centres of the scatterers were equally spaced $s = 1.2$ m. The material was assumed to be PVC, with compression wave propagation velocity $c_p = 2143$ m/s, shear wave propagation velocity $c_s = 875$ m/s, and density $\rho = 1400$ kg/m^3. The outer fluid was water, with sound wave propagation velocity $c_f = 1500$ m/s and density $\rho_f = 1000$ kg/m^3. Three configurations were considered based on the interior of the scatterers: *i*) water-filled; *ii*) air-filled, with sound propagation velocity 340 m/s and density 1.225 kg/m^3; and *iii*) state of vacuum.

The array of scatterers was subjected to a dilatational point source located in the fluid at position $\widetilde{\mathbf{x}}_0 = (-4.0, 0)$ (Figure 9). The incident wave field $\widetilde{p}^I$ was defined as in the previous section. The problem response of the fluid-structure system was studied for a frequency $f = 6400$ Hz.

The scatterers were modelled with spectral finite elements while outer and inner fluid subdomains were represented with the SBEM. The discretisation was chosen to enable a nodal density per wavelength of $d_\lambda = 12$ in the outer fluid, while the scatterers and the inner fluid meshes were defined to match the outer fluid mesh. The outer fluid was modelled with 34 elements, so the cylinders and the inner fluid were modelled

Table 1: Summary of the number of elements, n_{elem}, number of nodes n_{node} for both SBEM and SFEM, scaled L_2-error ϵ_2 of the total fluid pressure, horizontal and longitudinal solid displacement and CPU time, computed for the different hp discretisations.

	SBEM		SFEM				Scaled L_2 error ϵ_2			CPU time [s]
$1/h[\mathrm{m}^{-1}]$	n_{elem}	n_{node}	n_{elem}	n_{node}	p	d_λ	ϵ_2^p	$\epsilon_2^{u_x}$	$\epsilon_2^{u_z}$	
		16		57	2	5	2.1362×10^{-1}	2.2429×10^{-1}	5.7590×10^{-2}	0.526
		24		121	3	7.5	1.2179×10^{-2}	1.5760×10^{-2}	8.0715×10^{-3}	1.051
2.12	8	32	12	209	4	10	1.7836×10^{-3}	2.0796×10^{-3}	1.0771×10^{-3}	1.713
		48		457	6	15	5.7194×10^{-4}	4.9001×10^{-4}	1.0273×10^{-3}	4.379
		64		801	8	20	5.0114×10^{-4}	3.9949×10^{-4}	1.0014×10^{-4}	11.36
		32		209	2	10	3.9259×10^{-3}	5.4951×10^{-3}	3.9152×10^{-3}	0.899
4.24	16	48	48	457	3	15	1.2872×10^{-4}	3.0848×10^{-4}	2.3735×10^{-4}	2.018
		64		801	4	20	6.0030×10^{-5}	2.7535×10^{-5}	7.5524×10^{-5}	3.976
8.48	32	64	192	801	2	20	1.6663×10^{-4}	4.2036×10^{-4}	3.2369×10^{-4}	2.449

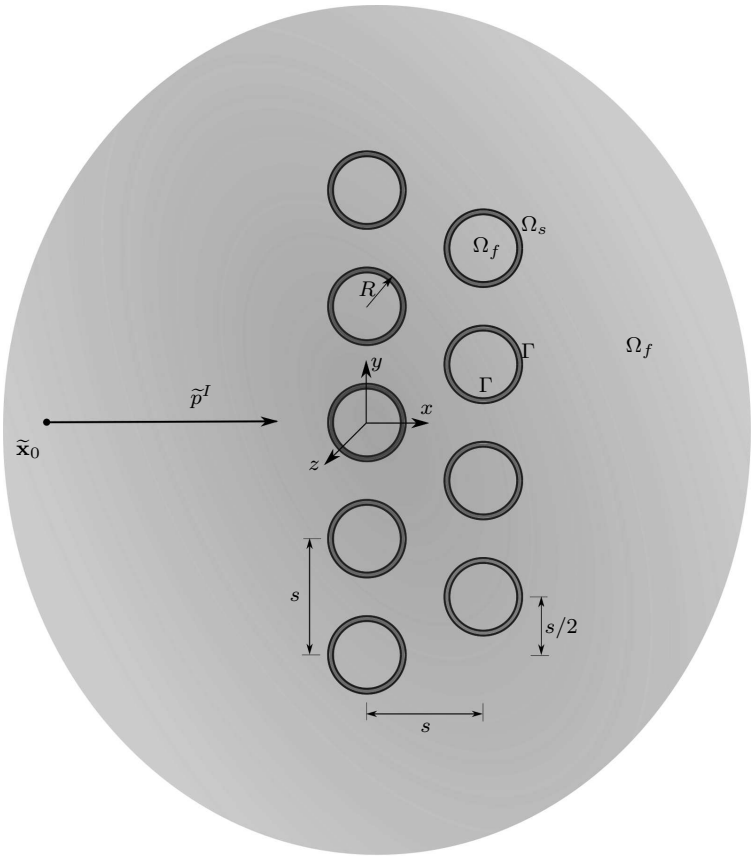

Figure 9: Configuration of scatterers.

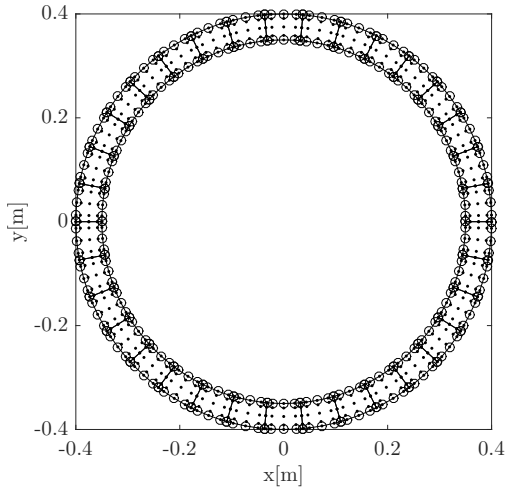

Figure 10: Scatter discretisation with $d_\lambda = 12$ and $\kappa_f h = 2$

again with 34 elements. The element order was set to $p = 4$ in all cases. This discretisation resulted in a nodal density $d_\lambda = 12$ with and $\kappa_f h = 2$ in the outer fluid. Figure 10 shows the discretisation of one scatter. The longitudinal wavenumber κ_z was not taken into account when computing the nodal density per wavelength.

The 3D solution was computed as the superposition of 2D problems with different longitudinal wavenumbers by means of Equation (6). The 3D solution can be computed in a set of regularly spaced points along the longitudinal direction where $\Delta z = 2\pi/\max\{\kappa_z\}$. The maximum wavenumber $\max\{\kappa_z\} = 160$ rad/m was chosen to compute the solution enabling six points in a longitudinal wavelength, $\Delta z = 2\pi/\max\{\kappa_z\} = 0.0393$ m. The maximum wavenumber $\max\{\kappa_z\}$ should be large enough to account for the slowest waves, namely guided waves, given by:

$$v_f = \frac{2\pi f}{\max\{\kappa_z\}}. \tag{50}$$

In this case, -160 rad/m $\leq \kappa_z \leq 160$ rad/m, so it is possible to account for waves with velocity higher than 250 m/s. The wavenumber sampling $\Delta\kappa_z = 0.5178$ rad/m allowed to compute the solution for a maximum distance $L = \pi/\Delta\kappa_z = 6.0672$ m from the source.

First, the behaviour of the cross section is analysed. Figure 11 shows the total pressure field in the outer fluid and the scattered pressure field inside the cylinders at a vertical plane $z = 0$ for the three studied cases. The total pressure fields are quite similar in the three cases. The maximum pressure was found at the source point and the scatterer configurations produced a shadowed zone, with a lower pressure amplitude. The vibration of the internal surface of the cylinders caused a scattered wave field inside them in the fluid-filled cases. When the cylinders were filled with water (Figure 9(a)), the scattered pressure field shows a distribution in accordance with the incident field, similar wavelength, amplitude, phase and direction, as the fluid properties were the same. The fluid-filled case (Figure 9(b)) exhibits a much more complex pattern,

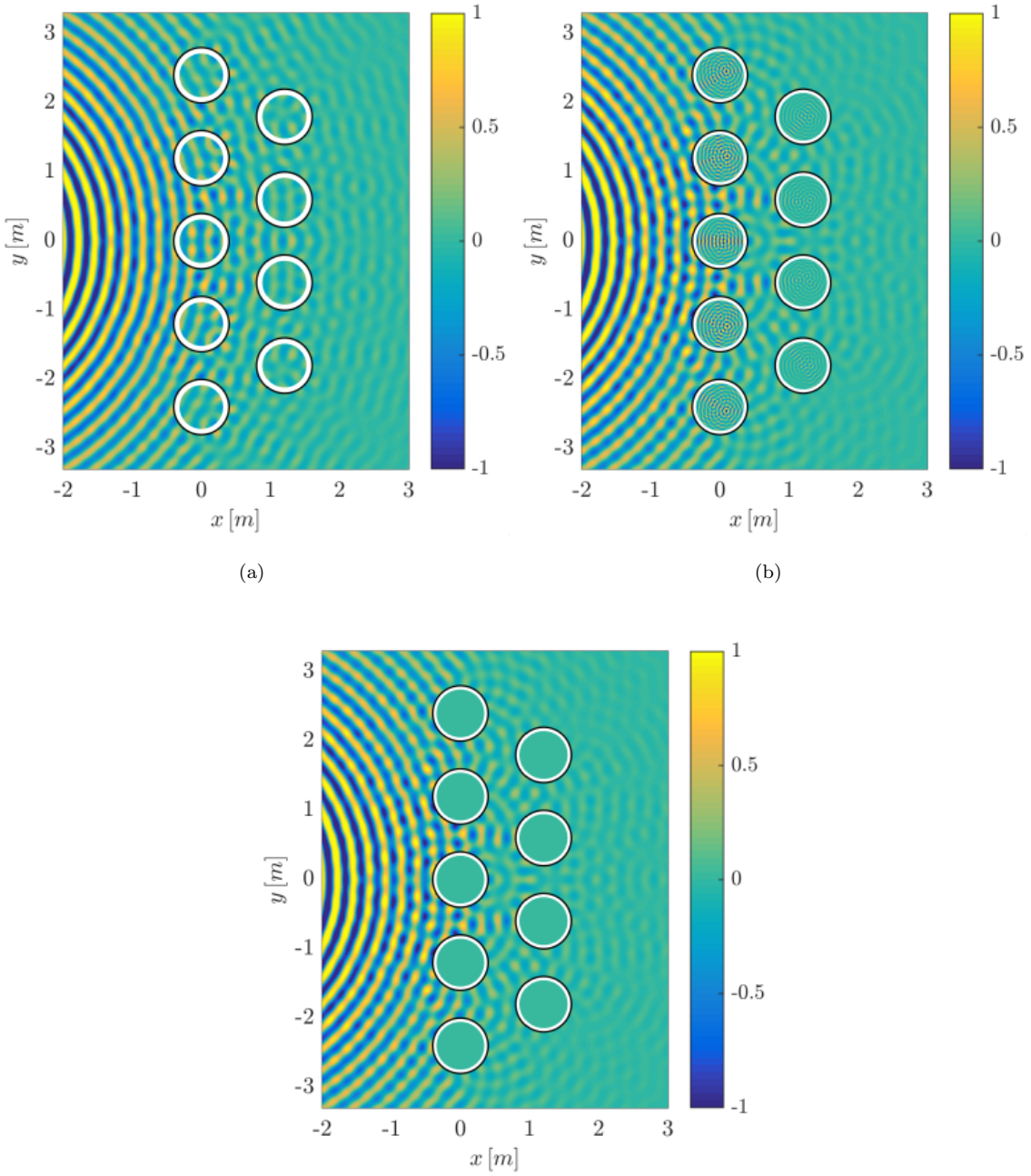

(a)

(b)

(c)

Figure 11: Real part of the pressure field at cross-section of the scatterers system at the vertical plane $z = 0$ for the (a) water-filled cylinders, (b) air-filled cylinders and (c) vacuum cylinders. Sound pressure in water medium was normalised to 0.15 Pa, and to 5×10^{-5} Pa in air medium.

with lower amplitude and wavelength and any concordance with the incident field in direction or phase due

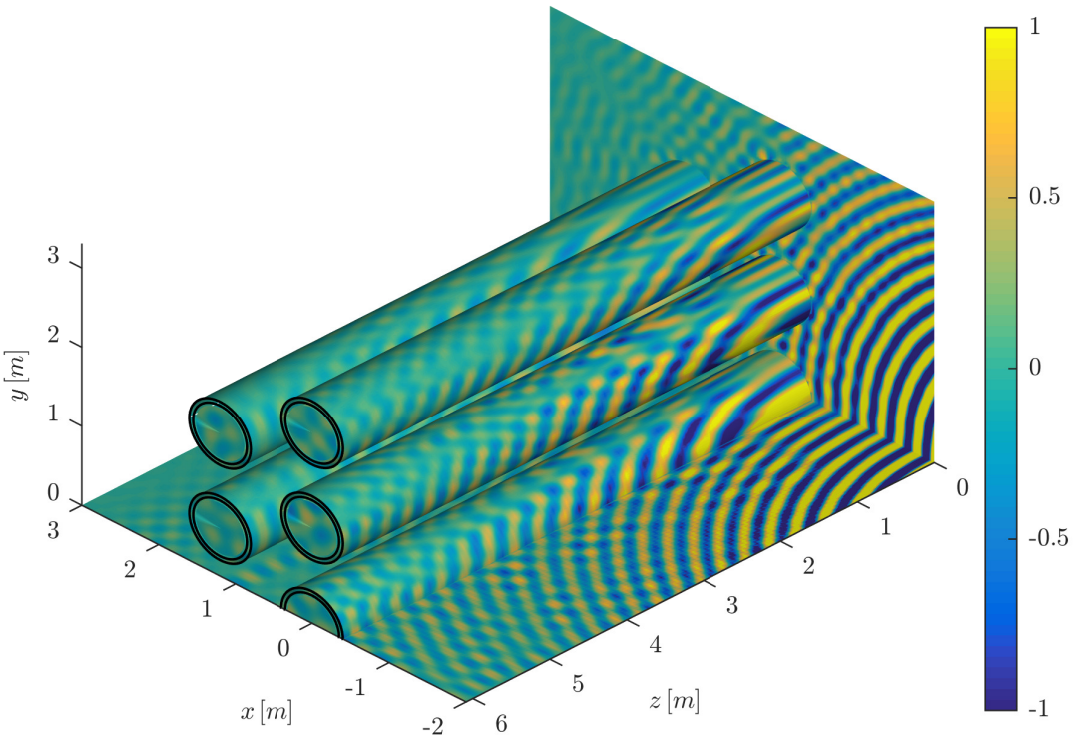

Figure 12: Real part of the pressure field (normalised to 0.15 Pa) in an unbounded fluid by a system of water-filled elastic scatterers.

to the difference in the properties of inner and outer fluids. The vacuum and air-filled systems presented the best attenuation, as the water-filled system allowed the waves to propagate through the scatterers.

Figure 12 shows the 3D representation of the sound pressure at the surface of the scatterers and the total pressure field in the fluid domain for the water-filled example. The scattered pressure field at a vertical plane $z = 6.0672$ m inside the cylinders is also shown. Only half of the model is represented for clarity's sake, because of problem symmetry. The pressure field had a spherical distribution centred at the source, which was progressively decreasing as the distance to the source increased. Figure 13 shows the deformed shape of the solid scatterers external surface and displays the normal displacement to the boundary in the colour scale. The displacement field also had a spherical distribution centered at the source, which decreased as the distance from the source increased. Maximum amplitudes of both the pressure and displacement were found at the plane $z = 0$, where the source was located and the incident field was higher.

This example has shown that the proposed method can be used to study the wave propagation in a fluid-filled elastic waveguides immersed in an unbounded acoustic medium. The proposed method was able to represent different fluid properties for the unbounded fluid and the acoustic enclosures.

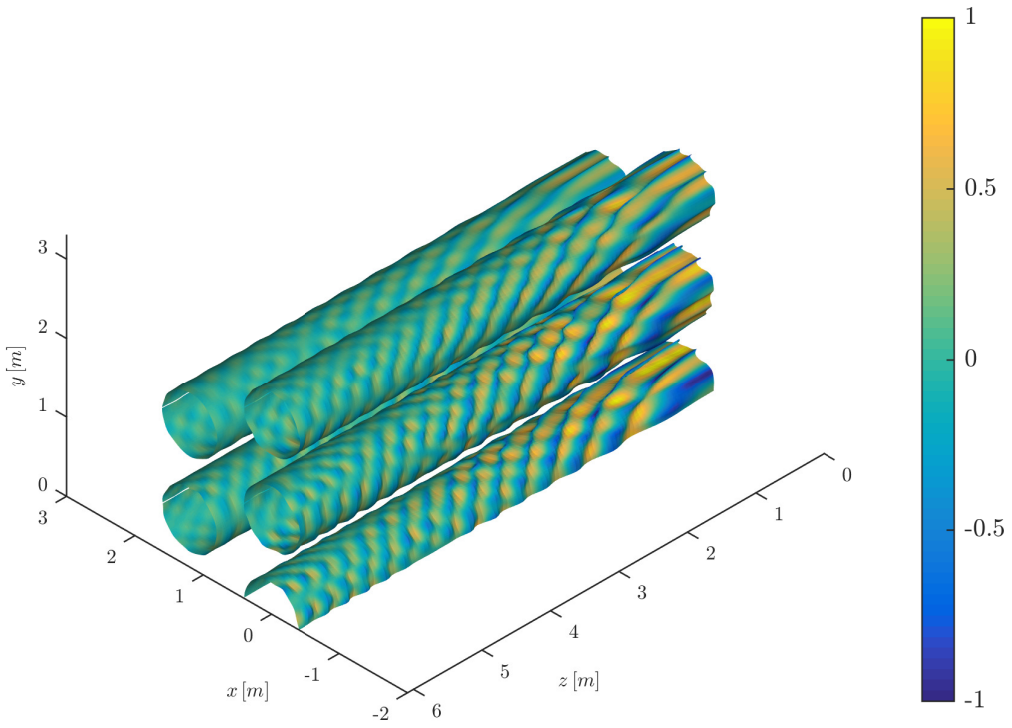

Figure 13: Real part of normal displacement at external surface (normalised to 1.2×10^{-12} m) in a system of water-filled elastic scatterers, represented over the deformed shape.

5. Conclusions

This work has proposed a spectral element formulation based on the BEM and the FEM to study fluid and solid wave propagation. The presented methodology looks at 3D problems whose materials and geometric properties remain homogeneous in one direction. Solid subdomains were modelled with the SFEM, whereas the unbounded fluid media and acoustic enclosures were represented by the SBEM. The coupling of both methods was carried out by imposing the appropriate boundary conditions at the interface to study fluid-structure wave propagation.

The model was verified with two benchmark problems with analytical solutions. The SBEM was verified with a problem involving wave propagation over an unbounded acoustic domain. The coupled SBEM-SFEM was verified with a problem concerning a cylindrical elastic waveguide in an unbounded fluid medium. Numerical results show good agreement with the analytical solution. An $h-p$ analysis shows that an optimal solution in terms of accuracy and computational effort can be obtained through an hp-refinement. Discretisations with a nodal density per wavelength of ten are enough to achieve reasonable accuracy. The accuracy improves by increasing the nodal density up to twenty. To conclude, we found that medium size discretisations gave as accurate results as coarse and fine meshes for the same nodal density per wavelenght, with lower computational cost.

Finally, the coupled methodology was used to study the wave field radiated by a three dimensional fluid-filled elastic scatterers system submerged in an unbounded acoustic medium. The sound pressure field and the scatterer's surface displacements were studied. The proposed method made it possible to represent different fluids for the unbounded medium and the acoustic enclosures.

Acknowledgements

The research work presented herein was supported by the Spanish Ministry of the Economy and Competitiveness (Ministerio de Economía y Competitividad) through research project BIA2016-75042-C2-1-R. It was also supported by project POCI-01-0247-FEDER-017759 (SmartCore – Desenvolvimento de painéis multifuncionais de elevada performance), funded by the Operational Program for Competitiveness and Internationalization (POCI) of Portugal 2020, with the support of the European Regional Development Fund (FEDER). Financial support is gratefully acknowledged. The authors also wish to acknowledge the support provided by the Andalusian Scientific Computing Centre (CICA).

References

[1] I. Babuška, F. Ihlenburg, E. T. Paik, S. A. Sauter, A Generalized Finite Element Method for solving the Helmholtz equation in two dimensions with minimal pollution, Computer Methods in Applied Mechanics and Engineering 128 (3) (1995) 325 – 359.

[2] F. Ihlenburg, I. Babuška, S. Sauter, Reliability of finite element methods for the numerical computation of waves, Advances in Engineering Software 28 (7) (1997) 417 – 424.

[3] A. A. Oberai, P. M. Pinsky, A numerical comparison of finite element methods for the Helmholtz equation, Journal of Computational Acoustics 08 (01) (2000) 211–221.

[4] C. Willberg, S. Duczek, J.M. Vivar Perez, D. Schmicker, U. Gabbert, Comparison of different higher order finite element schemes for the simulation of Lamb waves, Computer Methods in Applied Mechanics and Engineering 241-244 (2012) 246 – 261.

[5] A. T. Patera, A spectral element method for fluid dynamics: Laminar flow in a channel expansion, Journal of Computational Physics 54 (3) (1984) 468 – 488.

[6] W. Ostachowicz, P. Kudela, M. Krawczuk, A. Zak, Guided Waves in Structures for SHM: The Time - Domain Spectral Element Method, Wiley, 2012.

[7] G. Degrande, G. De Roeck, A spectral element method for two-dimensional wave propagation in horizontally layered saturated porous media, Computers & Structures 44 (4) (1992) 717 – 728, Special Issue: Computational Structures Technology.

[8] P. Z. Bar-Yoseph, D. Fisher, O. Gottlieb, Spectral element methods for nonlinear spatio-temporal dynamics of an Euler-Bernoulli beam, Computational Mechanics 19 (1) (1996) 136 – 151.

[9] A. Calaon, R. Adey, J. Baynham, A spectral boundary element method, in: A. Kassab, C. A. Brebbia, E. Divo, D. Poljak (Eds.), Boundary Elements XXVII, Vol. 39, WIT Press, 2005, p. 65.

[10] H. Holm, M. Maischak, E.P. Stephan, The hp-Version of the Boundary Element Method for Helmholtz Screen Problems, Computing, 57 (2) (1996) 105–134.

[11] W.S. Hwang, Boundary spectral method for acoustic scattering and radiation problems, Journal of the Acoustical Society of America, 102(1) (1997) 96–101.

[12] F. Zou, M.H. Aliabadi, On modelling three-dimensional elastodynamic wave propagation with boundary spectral element method, European Journal of Computational Mechanics, 27(3) (2018) 204–228.

[13] P. Kudela, M. Krawczuk, W. Ostachowicz, Wave propagation modelling in 1D structures using spectral finite elements, Journal of Sound and Vibration 300 (1) (2007) 88 – 100.

[14] C. Zhu, G. Qin, J. Zhang, Implicit Chebyshev spectral element method for acoustics wave equations, Finite Elements in Analysis and Design 47 (2) (2011) 184 – 194.

[15] T. R. Milind, M. Mitra, A Study on Fourier Spectral and Fourier-Hankel Spectral Field Variable Approximations in BEM for 2D Interior Helmholtz Problems, Procedia Engineering 144 (2016) 520 – 527, International Conference on Vibration Problems 2015.

[16] A. Cerrato, L. Rodríguez-Tembleque, J. A. González, M. H. Ferri Aliabadi, A coupled finite and boundary spectral element method for linear water-wave propagation problems, Applied Mathematical Modelling 48 (2017) 1 – 20.

[17] A. Romero, F.J. Cruz-Muñoz, A. Tadeu, P. Galvín, A novel 2.5D spectral approach for studying thin-walled waveguides with fluid-acoustic interaction, Computers and Structures 204 (2018) 1 – 19.

[18] F.J. Cruz-Muñoz, A. Romero, A. Tadeu, and P. Galvín, A 2.5D spectral approach to represent acoustic and elastic waveguides interaction on thin slab structures, Procedia Engineering 199 (2017) 1374–1379.

[19] A. Pereira, A. Tadeu, J. António, Influence of the cross-section geometry of a cylindrical solid submerged in an acoustic medium on wave propagation, Wave Motion 36 (1) (2002) 23–39.

[20] L. Gavrić, Computation of propagative waves in free rail using a finite element technique, Journal of Sound and Vibration 185 (3) (1995) 531 – 543.

[21] L. Gavrić, Finite element computation of dispersion properties of thin-walled waveguides, Journal of Sound and Vibration 173 (1) (1994) 113–124.

[22] M. Bouchon, K. Aki, Discrete wave-number representation of seismic-source wave fields, Bulletin of the Seismological Society of America 67 (1977) 259 – 277.

[23] J. Domínguez, Boundary elements in dynamics, Computational Mechanics Publications and Elsevier Applied Science, 1993.

[24] A. Tadeu, L. Godinho, Three-dimensional wave scattering by a fixed cylindrical inclusion submerged in a fluid medium, Engineering Analysis with Boundary Elements 23 (9) (1999) 745 – 755.

[25] B. Fornberg, J. Zuev, The Runge phenomenon and spatially variable shape parameters in RBF interpolation, Computers and Mathematics with Applications 54 (3) (2007) 379–398.

[26] T. W. Wu, Boundary Element Acoustics Fundamentals and Computer Codes, WIT Press, 2000.

[27] O. Zienkiewicz, The Finite Element Method,Third Ed., McGraw-Hill, 1986.